nature physics

SUPPLEMENTARY INFORMATION

DOI: 10.1038/NPHYS3714

Laser cooling and control of excitations in superfluid helium

I. SUPERFLUID HELIUM: TWO FLUID MODEL AND THIRD SOUND

Mechanical motion of liquid helium is described by the two-fluid model, where the liquid is composed of a normal fluid and a superfluid component that intermingle without any viscous interaction [1, 2]. This model gives several types of fluid motion such as first and second sound, where longitudinal pressure waves of the superfluid and normal fluid component are in phase and out of phase respectively. The mechanical motion studied here is that of third sound in superfluid helium-4, which refers to surface waves occurring on nanoscale films (~ 10 nm thick) [3–6]. In this case the film is so thin that the normal fluid component is viscously clamped to the substrate, leaving only the superfluid component free to oscillate perpendicular to the substrate. Third sound is completely analogous to the classical treatment of shallow water waves; however, the presence of superfluidity is necessary for nanoscale films because such waves are quickly attenuated within the normal fluid component.

For third sound waves the restoring force is provided by the van der Waals interaction of the helium with the substrate. The resulting mechanical oscillations have a velocity (c_{s}) that is highly dependent on the thickness of the superfluid layer [3]:

$$c_{\mathrm{s}} = \sqrt{3\frac{\rho_s}{\rho}\frac{\alpha_{\mathrm{VDW}}}{d^3}}, \tag{1}$$

where ρ_s/ρ is the ratio of superfluid to total fluid density, and α_{VDW} is the van der Waals coefficient ($\alpha_{\mathrm{VDW}} = 2.65 \times 10^{21}$ nm^{5}s^{-2} for helium on a silica substrate [7]). This third sound velocity, combined with a confining geometry and associated boundary conditions, defines the frequency and mode shapes of third sound resonators.

The properties of third sound in superfluid helium-4 has been experimentally probed since its discovery in the late 1950's [3–6]. Measurement techniques have involved superconducting bolometers [8, 9], optical ellisometry [10], and resonant circuit capacitive readout [11–13]. These techniques contributed greatly to the understanding of superfluid thin film dynamics, for example thermal transport properties, vortex formation and 2-D phase transitions. However the measurement rate, as defined in forthcoming sections, of these experiments has not been sufficient to track the amplitude of the intrinsic thermal fluctuations residing within the film in real-time.

DOI: 10.1038/NPHYS3714

II. THIRD SOUND MODE SHAPES

The characteristic eigen-modes of simple confining geometries can be calculated analytically. Taking a cylindrically symmetric film, roughly matching the more complex microtoroidal geometry of our experiments, the eigen-frequencies can be calculated using separation of variables in cylindrical coordinates (r, ϕ) [11, 14], giving a general solution based on a Bessel function of the first kind:

$$\Phi(r, \phi, t) = \sum_{m,n} \Phi_{m,n} J_m(\omega_{m,n} r/c) \exp(im\phi) \exp(-i\omega_{m,n} t) \tag{2}$$

where m and n represent azimuthal and radial mode number respectively, $J_m(\omega_{m,n} r/c)$ is the Bessel function and $\Phi_{m,n}$ is the oscillation amplitude. This general solution applies to both "free" and "fixed" boundary conditions (Neumann and Dirichlet conditions respectively) with the characteristic mode shapes distinctly different between the two. In the context of superfluid third sound resonators the appropriate boundary condition is not typically known from first principles but rather inferred from the measured frequencies of the mode spectrum. While numerous superfluid experiments have reported fixed boundary conditions [11, 12, 14, 15], mode spectra consistent with free boundary conditions have also been widely observed [13, 15–17].

To further illustrate the resonant modes we first consider a fixed boundary condition (Dirichlet condition) where the displacement is zero at the periphery $\Phi(R, \phi, t) = 0$. Therefore the Bessel function must be $J_m(\omega_{m,k} R/c) = 0$, hence enforcing the argument $(\omega_{m,k} R/c)$ to equal a zero of J_m, namely $\omega_{m,n} R/c = \zeta_{m,n}$ where $\zeta_{m,n}$ is the nth zero (e.g $\zeta_{0,1} = 2.405$, $\zeta_{1,1} = 3.832$ and $\zeta_{0,2} = 5.5201$). If the boundary condition is free (Neumann condition), also known as the "no flow" condition due to a mass conservation argument [15], then the radial derivative of the displacement is zero $\partial_R \Phi(R, \phi, t) = 0$ [15]. Therefore the derivative of the Bessel function must then be $J'_m(\omega_{m,k} R/c) = 0$, hence enforcing the argument $(\omega_{m,k} R/c)$ to equal a zero of J'_m, namely $\omega_{m,n} R/c = \zeta'_{m,n}$ where $\zeta'_{m,n}$ is the nth zero (e.g $\zeta'_{0,1} = 3.8317$, $\zeta'_{1,1} = 1.841$ and $\zeta'_{0,2} = 7.016$). The first few mode shapes and relative resonant frequencies with these two boundary conditions for a cylindrically symmetric system are shown in Fig. 1(a,b).

In general, for all but the simplest geometries the characteristic mode shapes and boundary conditions are non-trivially determined by various experimental factors, for example film thickness, temperature, surface roughness, confining geometry and van der Waals coefficients. Furthermore, geometries more complicated than a simple disk will support a denser spectrum of third sound

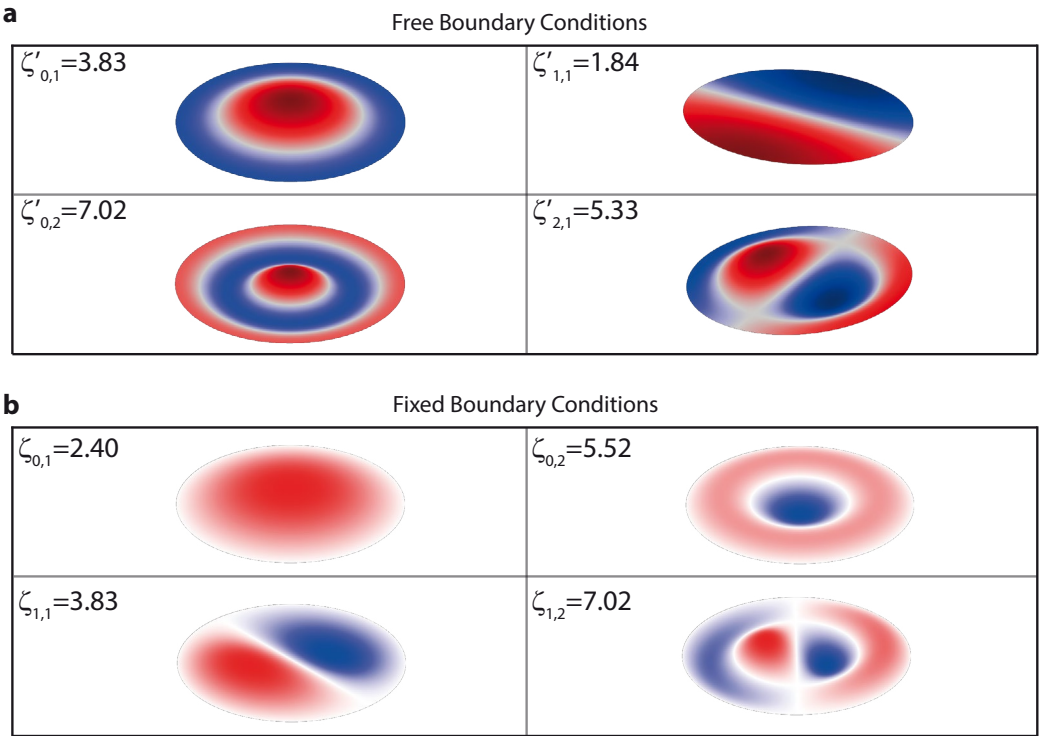

FIG. 1: **Modes of cylindrically symmetric third sound resonator** (**a**) Displacement profile with free boundary conditions. (**b**) Displacement profile with fixed boundary conditions. The coefficients in the top left corner of each box are the nth zero to the mth order Bessel function and its derivative, $\zeta_{m,n}$ and $\zeta'_{m,n}$ respectively. Colour code: Red (blue) shaded region represents positive (negative) displacement and white regions represents no displacement.

modes. In this context, finite-element-modelling (FEM) of third sound on a microtoroid (major radius $34\ \mu$m, minor radius $3\ \mu$m) reveals a dense spectrum of modes, illustrated in Fig. 2. The height of each mode is normalised by its amplitude at the perimeter of the microtoroid to give an estimate of the relative optomechanical coupling strengths. This results in a density of observable modes consistent to that seen in our experiments. The displacement profile extracted from FEM also provides a heuristic understanding of the groups of modes supported by the structure. For example the disk that connects the microtoroid to the pedestal will support drum head modes similar to those seen in Fig. 1. Illustrations of these modes on a microtoroid is seen in the insets to Fig. 2, with modes appearing on both the top and bottom sides of the disk. For these types of modes, a fraction of the film fluctuations will "leak" from the disk to the outer torus, with close proximity to the optical evanescent field enabling optical readout. The drum head modes on the top and bottom

DOI: 10.1038/NPHYS3714

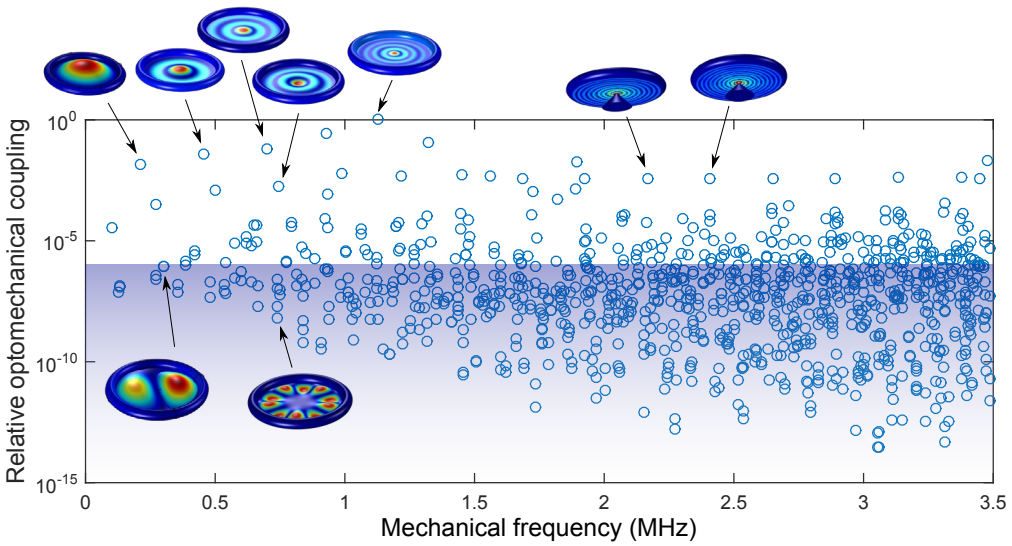

FIG. 2: **Dense third sound mode spectra of microtoroidal geometry.** FEM simulation of the relative optomechanical coupling rate of the first 1000 third sound modes supported by the microtoroid (Major radius 34 μm, minor radius 3 μm) covered in a superfluid film. The coupling rate is calculated by integrating the mechanical displacement around the periphery of the microtoroid, then normalised to the mode of highest optomechanical coupling. The shaded region indicates modes unlikely to be observed in our experiment. Insets: Example mode shapes of selected modes.

sides of the disk will also be coupled to each other through the continuous superfluid film that connects them. This coupling results in hybridization of some modes depending on mode shape, film thickness and specific microtoroidal geometry.

As such, the mode order and spacing is strongly geometry dependent, resulting in FEM simulations that cannot reliably identify specific experimentally observed modes. This issue, among others, further complicates calibrating the optomechanical coupling rate, which will be further discussed in the next section. It should also be noted that the mechanical dissipation rate has not been calculated, therefore the relative optomechanical coupling rate cannot be related to the experimentally observed signal-to-noise-ratio.

A. Superfluid film mass

Self-assembling superfluid helium thin films can exhibit very low masses compared to other microscale mechanical oscillators, thanks to a combination of nanometer-scale thickness and superfluid helium's low density ($\rho \simeq 145$ kg/m^3). For instance, in our experiments the superfluid film formed on the top of the microtoroid resonator whose mechanical modes are shown in Fig. 2 has a mass on the order of just a few picogram ($\sim$2 pg with a 3 nm thick film). This mass could be significantly reduced by utilising a resonator with smaller surface area, and/or a thinner film: third sound has been experimentally observed in superfluid helium films as thin as 2 atomic monolayers [7]). As an example, a still reasonably thick superfluid film of 1 nm formed on the top surface of a 1 micron radius whispering gallery mode resonator [18] would constitute a third sound resonator with a mass of only 450 attograms.

III. OPTOMECHANICAL COUPLING RATE

The relative optical frequency shift incurred from superfluid condensation can be estimated by comparing the total optical energy to that contained within the superfluid film [19]

$$\frac{\Delta\omega}{\omega_0} = -\frac{1}{2}\frac{\iiint_{He}(n_{He}^2-1)|E_0(\vec{r})|^2\mathrm{d}\vec{r}}{\iiint_{\mathrm{all}} n^2(\vec{r})|E_0(\vec{r})|^2\mathrm{d}\vec{r}} \tag{3}$$

where $n(\vec{r})$ is the spatial refractive index profile experienced by the unperturbed the electric field $E_0(\vec{r})$ (i.e. in the absence of superfluid). The refractive index of the superfluid is given by n_{He} with the integral in the numerator only evaluated over the volume of the superfluid layer, in contrast to the integral in the denominator which is taken over all space. Considering the fundamental mode of a microtoroidal resonator (major radius $35\ \mu$m, minor radius $3.5\ \mu$m) the optical frequency shift per nanometer of superfluid is estimated to be $-290\mathrm{MHz\ nm}^{-1}$.

To calculate the optomechanical coupling rate of a specific mode an overlap integral between the optical and mechanical mode must be performed. In the limiting case of simple geometries FEM allows a straightforward method to perform this calculation. However, as mentioned in the previous section, FEM of a microtoroid yields a dense spectrum of mechanical modes that prevents reliable identification of individual superfluid and optical modes. It should be noted that this situation is not unique in optomechanics with many systems utilizing experimental methods for calibration, for example by applying a known phase modulation onto the injected optical field.

DOI: 10.1038/NPHYS3714

This coherent modulation can then be used as a reference signal to determine the systems sensitivity to phase, and hence position, fluctuations [20]. A prerequisite of this technique, and many other calibration techniques, is an accurate measurement of the thermomechanical occupation. This measurement is unavailable in our superfluid system since the thermomechanical occupation does not depend on the cryostat temperature but rather an optically pumped non-equilibrium bath that raises the mode temperature above that of the cryostat (See Sec. V for further information). Even with launched optical powers as low as $5\ \mathrm{nW}$ we found the superfluid mode temperature to be dominated primarily by the non-equilibrium-bath.

Yet another method to extract g_0 is to fit the measured modification of the mechanical resonance frequency and dissipation rate with optical detuning to the theory for dynamical backaction with g_0 as the free parameter [21]. However, this technique breaks down with the inclusion of additional processes that also exhibit their own dynamical backaction. In our case this additional process is the photothermal force which acts to obscure the the radiation pressure effects, hence preventing the calculation of g_0. In other photothermal systems this problem is typically alleviated by either a lock-in detection scheme over a large frequency range [22, 23] or by isolating the radiation pressure and photothermal responses and independently calibrating each one [24]. For our superfluid system the large frequency span modulation technique was obscured by a dense spectrum of superfluid modes, furthermore we were unable to independently isolate the radiation pressure and photothermal effects due to the intrinsic nature of both effects to superfluid helium.

In the context of extracting g_0 using measurements of dynamical backaction, it should be noted that the observation of quantum backaction (zero optical detuning) would also allow such calibration. This regime is only reached in the situation of high optomechanical coupling rate [25] and requires precise thermometry of the mechanical mode versus laser power. We performed such thermometry and found our superfluid system is not in the quantum backaction dominated regime (see Sec. V for further details).

IV. EXPERIMENTAL DETAILS

Our experiment is contained inside a sealed sample chamber which is mounted within an Oxford Instruments closed cycle helium-3 cryocooler with a base temperature of 300 mK. Inside the sample chamber the microtoroid is mounted on Attocube translation stages for linear positioning relative to the tapered optical fibre, which itself is mounted on a custom made glass taper-holder

to match the thermal contraction/expansion during thermal cycling. Imaging of the microtoroid and taper is achieved via mounted microscopes directed through a set of windows fixed into the bottom of the cryostat. A stainless steel access tube connected to the sample chamber is used to introduce helium-4 gas into the sample chamber.

Vibrations from the continuously running pulse-tube cooler (PTC) are transmitted through the cryostat to the sample chamber, preventing stable positioning of the taper-toroid separation. To circumvent this issue, on-chip stabilization beams are added using photolithography during the fabrication of the microtoroid. With one beam located on either side of the microtoroid the taper may "rest" upon the beams, making the relative vibration common-mode and stabilizing the separation to a high precision (similar to that used in Ref. [26]). This makes it possible to indefinitely maintain critical coupling even while the PTC is operational. Vibrations from the PTC does not have any effect on the microtoroid modes; however, it can drive the motion of the superfluid modes. To prevent this we perform measurements on the superfluid with the PTC switched off. To minimize light scattering out of the taper mode the support beams are only 5 μm wide and selectively thinned from 2 μm to less than 500 nm.

By measuring the optical resonance frequency of the microtoroid as the cryostat temperature is decreased we were able to observe formation of the superfluid film on the microtoroid (see Fig. 3). As mentioned in the previous section we calculate that the superfluid film will cause the optical resonance frequency to shift by -290 MHz nm^{-1}. Above the superfluid transition temperature the optical frequency shift is independent of the helium pressure and is due to thermal expansion of the microtoroid and the thermorefractive effect [27]. Below the superfluid transition temperature the optical frequency shift is larger for higher gas pressures as this results in a thicker superfluid film forming on the microtoroid surface. Increasing the helium pressure from 45 mTorr to 91 mTorr results in an extra optical shift of -457 MHz at 600 mK; thus, an increase in thickness of the superfluid layer of $457/290 = 1.58$ nm.

Ultrasensitive readout of the phase fluctuations imprinted by the motion of the superfluid film is achieved via homodyne detection using a fibre interferometer. The motion of the third sound waves was observed using both spectral and network analysis. Fig. 4a shows a typical mode spectrum acquired via network analysis, showing the large range of third sound modes present in our system. Note that the network analysis measurements were obtained by optically driving the mechanical modes and measuring the response. The response of the mechanical modes was measured as the drive strength (optical modulation depth) was increased. At high drive powers the superfluid

DOI: 10.1038/NPHYS3714

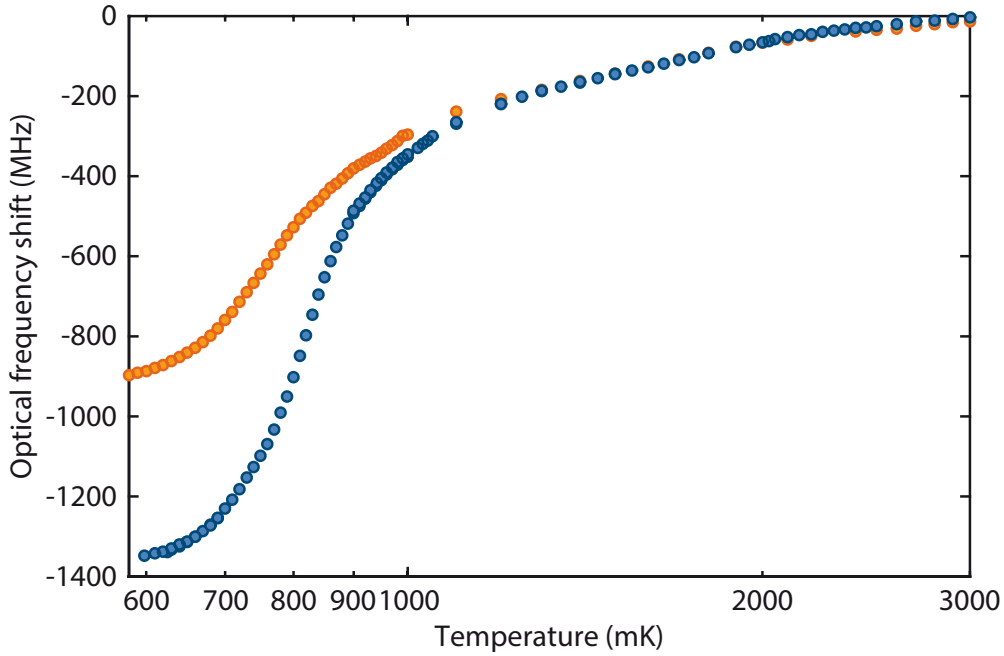

FIG. 3: **Optical frequency shift.** Measured frequency shift of the optical mode as the cryostat temperature is changed from 600 mK to 3 K for two different helium gas pressures in the sample chamber. Orange circles - 45 mTorr, blue circles - 91 mTorr (both measured with the cryostat at 2.8 K).

modes were observed to exhibit a Duffing nonlinearity[12, 28]; therefore, for all network analysis measurements care was taken to ensure the drive strength was well below that required to observe the nonlinearity such that all measurements were performed in the linear regime. We note, further, that the largest frequency shifts observed due to Duffing nonlinearity, even in the presence to strong optical driving, were smaller than 1 % of the mechanical resonance frequency. Consequently, even had we utilised strong driving for the data in Fig. 2b of the main text, the modification due to the Duffing nonlinearity would be negligible.

To lock the relative phase angle between the local oscillator and signal we generate a 200 MHz amplitude modulation before the microtoroid. Mixing down the AC component of the photocurrent at the modulation frequency then provides a phase dependent error signal for the interferometer that is filtered and applied to a piezoelectric fibre stretcher. In this configuration the DC component also provides a dispersive error signal for the cavity lock which is enhanced by the local oscillator, enabling stable operation even with nanoWatts of optical power in the signal arm of the interferometer.

A series of measurements were made to confirm that the mechanical modes that we observed

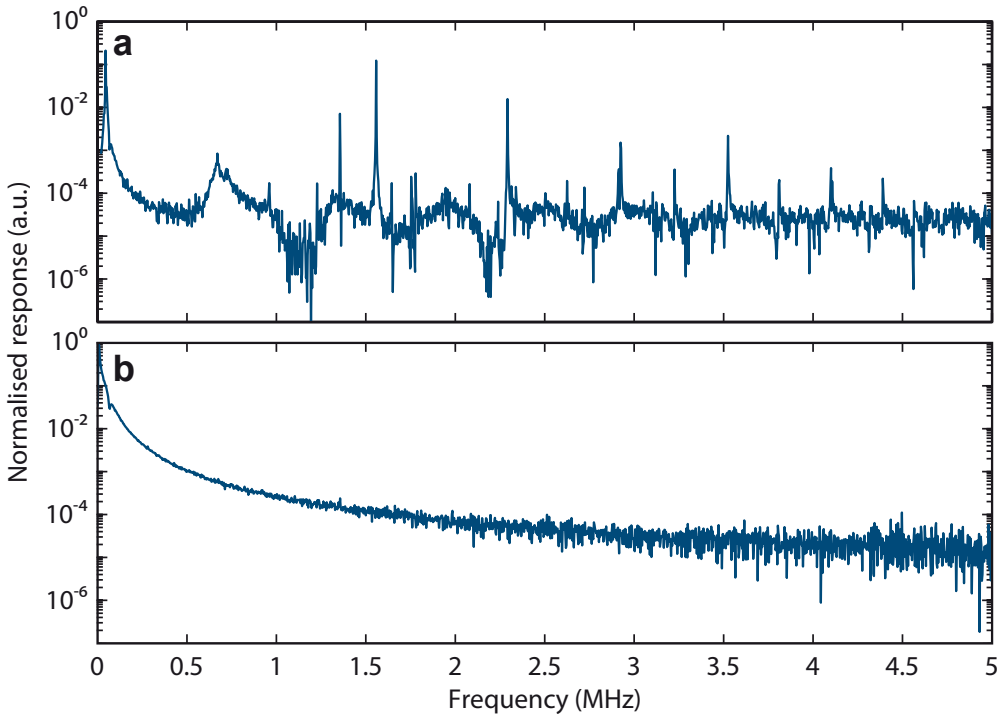

FIG. 4: **Superfluid mode spectrum.** (**a**) Network analysis measurement showing the spectrum of third sound modes present in our resonator at 900 mK. Each peak in the spectrum corresponds to a different third sound mode. (**b**) Network analysis measurement at a temperature above the superfluid transition temperature (1100 mK). Note the third sound modes are no longer observed. The large network response observed at low frequencies is due to the thermo-optic response of silica, which is known to reduce significantly with the formation of a superfluid helium layer[27, 29]

were in fact third sound modes in the helium film and not some other oscillatory mechanism. Network analysis was performed on the system with the cryostat temperature both below (Fig. 4a) and above (Fig. 4b) the superfluid phase transition temperature (1 K with 69 mTorr helium gas pressure - see Fig. 7). Below the superfluid transition temperature a large number of modes appear, which we attribute to resonances in the superfluid film. To further investigate this, network analysis measurements were made at 0.2 mK intervals over the superfluid transition (Fig. 5), with the superfluid modes appearing rapidly over this narrow temperature range. We also made measurements of the superfluid mechanical mode frequencies as the cryostat temperature is varied and compared this to the resonance frequency of a microtoroid mechanical mode (Fig. 6a). The superfluid mode frequencies decrease rapidly with temperature as the superfluid film increases in thickness (see Eq. 1) and then plateau as all of the helium has been condensed. In contrast, the

DOI: 10.1038/NPHYS3714

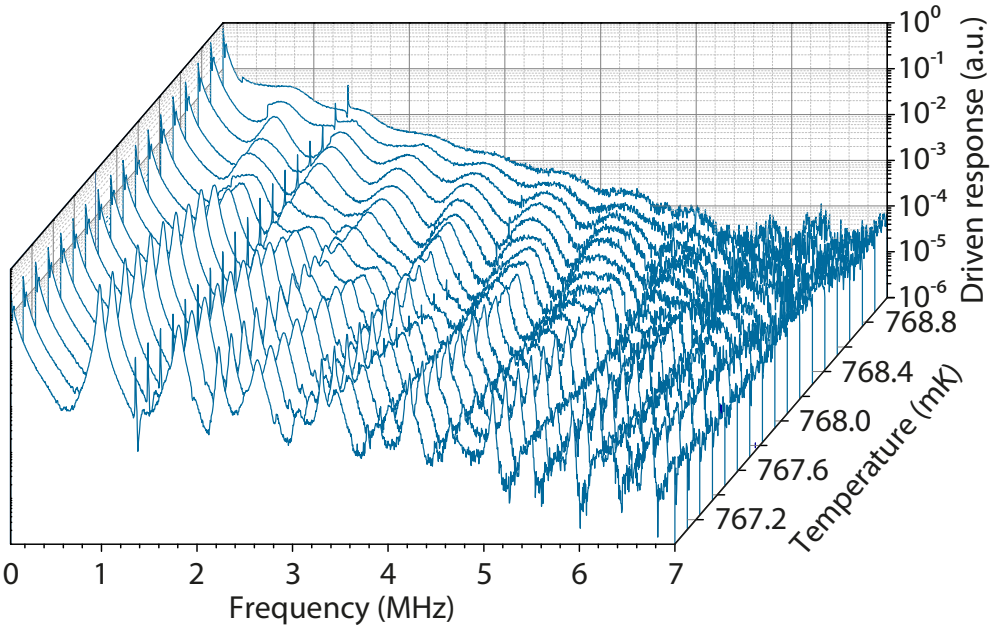

FIG. 5: **Superfluid mode spectra as temperature is varied.** Network analysis measurement showing the spectrum of third sound modes present as the cryostat temperature is varied over the superfluid phase transition (from 767 to 769 mK). Each peak in the spectrum corresponds to a different third sound mode aside from the much narrower peak at 1.35 MHz which is a mechanical mode of the microtoroid. The linewidth rapidly increases and response of the mode decreases as the temperature changes by 2 mK, until there is no longer any superfluid present and the superfluid modes are no longer visible. Note this data was taken for a helium gas pressure of 19 mTorr at 2.8 K, which is why the transition temperature is lower than for other data in this work (most data was taken at 69 mTorr at 2.8 K).

resonance frequency of the microtoroid mode varies by less than 0.1% over the same temperature range. Interestingly, we do not observe any interference, or anti-crossings, or change in dissipation rates as the frequency of the superfluid modes overlaps that of the microtoroid mode. Further, measurements were made of the resonance frequency of a superfluid mode as the pressure of helium gas inside the sample chamber was increased (Fig. 6b). As expected, increasing the helium pressure caused the frequency of the superfluid mode at base temperature to decrease, as the final thickness of the superfluid film is higher due to their being more helium atoms in the sample chamber. Also, higher pressure results in a higher superfluid transition temperature, as expected from the helium-4 phase diagram [6] (see Fig. 7).

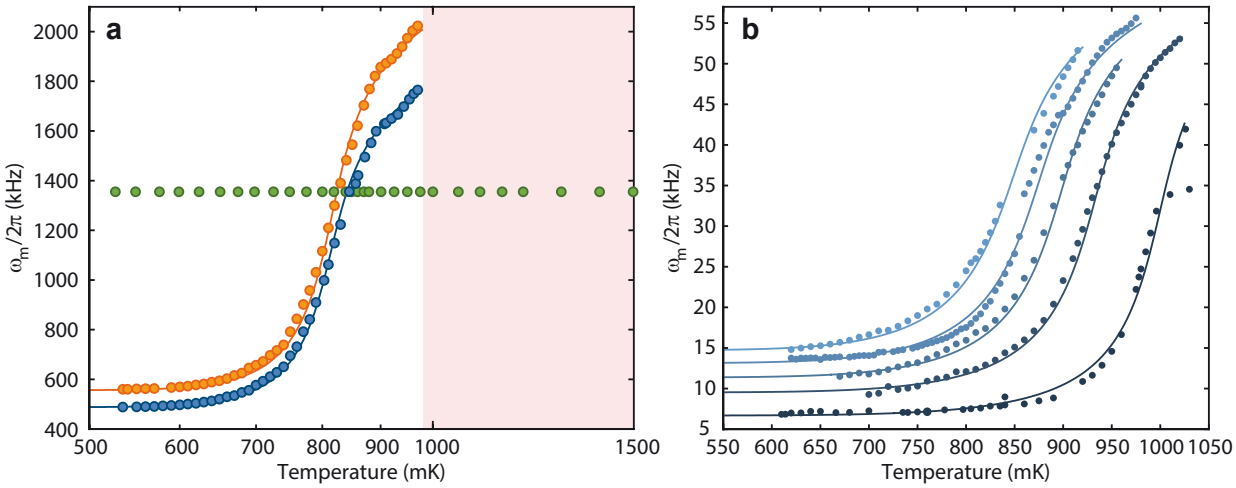

FIG. 6: **Mechanical resonance frequency vs temperature.** (**a**) Resonance frequency of two different superfluid third sound modes (blue and orange) and a microtoroid mechanical mode (green) as the cryostat temperature is varied. The blue and orange lines are a theoretical fit derived from modelling the condensation of the helium gas. The apparent roll-off in these curves at a temperatures above ≈900 mK is due to the nonlinear dependence of both the pressure at which the vapour-superfluid phase transition occurs (see Fig. 7) and third sound speed as a function of temperature. The pink shaded region shows the temperature region where there is no superfluid present, the helium is all in its gaseous state. (**b**) Resonance frequency of a third sound mode as the cryostat temperature is varied for different pressures of helium-4 gas in the sample chamber. The pressure of helium gas inside the sample chamber increases from the lightest blue plot (low pressure) to the darkest blue plot (high pressure). For higher gas pressures it is observed that the superfluid transition temperature is higher as expected from the helium-4 phase diagram (see Fig. 7). Further, the final mode frequency is lower for higher pressure as there are more gas molecules in the sample chamber, meaning the final film thickness is higher (see Eq. (1)). Note the mechanical mode measured in (**b**) is different than the mechanical modes measured in (**a**).

V. NON-EQUILIBRIUM BATH COUPLING

As commented in the main Letter, it is well-known that dynamical backaction due to detuned laser driving in a cavity optomechanical system can allow heating or cooling of the mechanical motion. In this section, we investigate the effects of the optical probe on the superfluid modes with the laser locked to the cavity resonance, in the absence of dynamical backaction. Specifically, spectral analysis was performed on two superfluid modes with resonance frequencies of 522.5 kHz

DOI: 10.1038/NPHYS3714

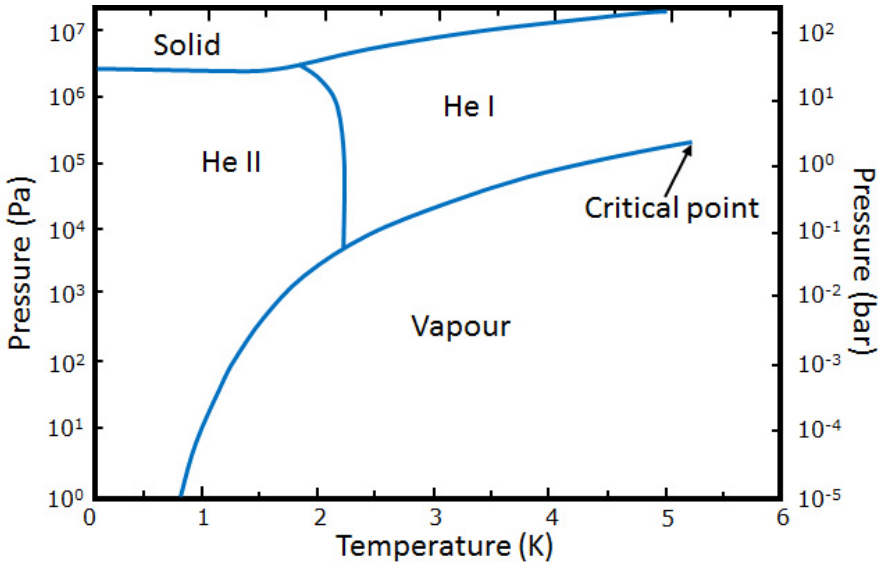

FIG. 7: **Helium-4 phase diagram.** Helium-4 phase diagram showing the vapour, solid, normal fluid (He I) and superfluid (He II) phases as a function of temperature and pressure. Data taken from Ref. [6].

and 482 kHz, as the coupled laser power was varied from $7 - 250$ nW. This measurement allows modifications of the mechanical resonance frequency, dissipation rate, and mode energy to be measured as function of optical power.

In these experiments we observe an increase in mode energy, equivalent to heating, of the superfluid mode. This increase in mode energy is characterized by a power law scaling of $P^{0.60}$ for the 482 kHz mode and $P^{0.69}$ for the 522.5 kHz mode (Figs. 8a, b). This non-integer power scaling of mode energy is markedly different to the linear power scaling expected if the temperature increase was due to quantum backaction or bulk heating of the superfluid. Concurrent to the increase in mode energy, it was observed that for both modes the mechanical linewidth increases with increasing laser power (Fig. 8c) and the mechanical resonance frequency decreases with increasing laser power (Fig. 8d). It should also be noted that we have observed behaviour that we attribute to boiling off of the superfluid layer, that is, for high laser powers the superfluid modes rapidly broaden and increase in frequency until they are no longer observable. However this occurs at laser powers greater than 5 μW, over an order of magnitude higher than the powers used in experiment.

To further rule out bulk heating effects, temperature characterisation measurements were performed on an intrinsic mechanical mode of the microtoroid itself at 1.35 MHz. It was not possible to perform these measurements directly using a third sound mode due to the considerable changes

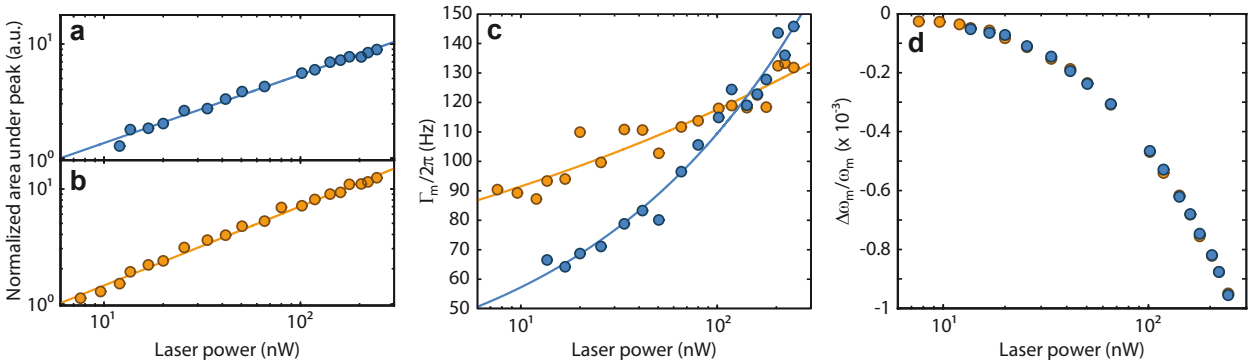

FIG. 8: **On-resonance behaviour.** Optical power dependence of the mechanical properties of a superfluid mode at 522.5 kHz (orange circles) and another at 482 kHz (blue circles), when the laser is locked to the cavity resonance. Measurements are performed with the laser coupled to a microtoroid optical mode at 1555.1 nm. (**a, b**) Measured thermal energy of the superfluid mode versus input laser power. The blue line is a power-law fit to the 482 kHz mode with scaling $\propto P^{0.6}$. The orange line is the fit to the 522.5 kHz mode with scaling $\propto P^{0.69}$. (**c**) Mechanical linewidth ($\Gamma_{\rm m}/2\pi$) versus optical power. The blue line is a power-law fit given by $\Gamma_{\rm m}/2\pi = 16.0 \times P^{0.38} + 19.3$ and the orange line is the fit $\Gamma_{\rm m}/2\pi = 49.2 \times P^{0.14} + 23.4$. (**d**) Relative shift in mechanical resonance frequency versus laser power. This shift to lower frequencies as the laser power is increased is likely due to the density of the superfluid component decreasing as the film is heated, decreasing the third sound speed (see Eq. 1)[30].

as the cryostat cools in the third sound resonance frequencies and dissipation rates, as well as the thickness of the superfluid film and therefore mode shapes, optomechanical interaction strengths, and photothermal interactions. In the case of an intrinsic microtoroid mode, the thermal energy of the mechanical mode, dissipation rate, and resonance frequency were all found to be independent of the laser power when varied from 7 nW to 250 nW whilst on-resonance. After confirming that on-resonance probing does not heat the mechanical modes of the microtoroid, we varied the temperature of the cryostat from 10 K to 600 mK with fixed optical power (100 nW). From the linear fit to data in Fig. 9 we found that the temperature of the microtoroid closely follows that of the cryostat.

To investigate the effect of coupling to a generalized non-equilibrium bath we first assign an effective temperature $T_{\rm B}\left(\omega\right) = \frac{\hbar\omega}{k_B}\left[\ln\left(\frac{S_{BB}(\omega)}{S_{BB}(-\omega)}\right)\right]^{-1}$ to the bath, where S_{BB} is the corresponding noise spectral density[31]. Since this non-equilibrium bath is independent to the thermal bath ($T_{th} \propto k_B T$), then the associated coupling rate is not given by the intrinsic decay rate (Γ_0), but

DOI: 10.1038/NPHYS3714

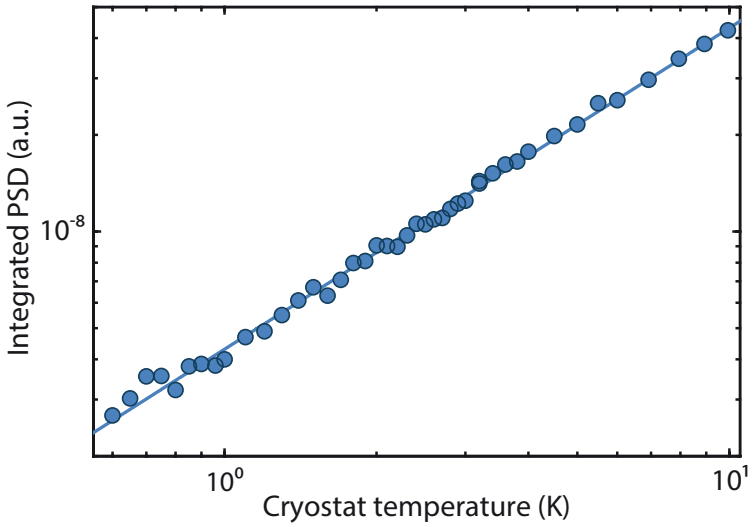

FIG. 9: **Microtoroid thermometry.** The mode energy, proportional to the integrated power spectral density (PSD), of a microtoroid mechanical mode at 1.35 MHz as the cryostat temperature is increased. The solid line is a linear fit to the experimental data showing there is good thermal anchoring of the microtoroid to the cryostat.

by the generalized expression $\Gamma_{\rm B} = \frac{x_{\rm zpf}^2}{\hbar^2}\left(S_{BB}\left(\omega_m\right) - S_{BB}\left(-\omega_m\right)\right)$ [31]. Taking the high quality factor limit gives the final temperature of the oscillator due to the presence of the thermal bath and the non-equilibrium bath:

$$T_{\rm Final} = \frac{T\Gamma_0 + T_{\rm B}\Gamma_{\rm B}}{\Gamma_0 + \Gamma_{\rm B}}. \tag{4}$$

Depending on how the non-equilibrium bath is excited via the optical field, specifically the ratio of $S_{BB}(-\omega)$ to $S_{BB}(\omega)$, it is possible to obtain linewidth narrowing or broadening in concert with increased mode energy. Further, we note that even though the optical field acts as a bath which couples to the superfluid this does not preclude us from studying its thermodynamic properties. The superfluid is still in thermal equilibrium, but at an elevated temperature when compared to the cryostat. It should be noted that a non-equilibrium bath is quite commonly found to limit the final temperature of a cryogenic micromechanical system [32, 33]. For example, Ref. [32] reported a mechanical mode temperature of $270\ \mathrm{mK}$, probed with as little as $\langle n\rangle = 0.016$ intracavity photons, for an optomechanical crystal in a dilution fridge at $10\ \mathrm{mK}$. Furthermore, Ref. [32] showed that the bath temperature may depend nontrivially on the coupled laser power, resulting in a final mode temperature that permits the non-integer power law scaling behaviour we observe in Fig. 8.

VI. THEORETICAL TREATMENT OF PHOTOTHERMAL INTERACTION

Here we will theoretically explore the situation of generalized optomechanical coupling with both radiation pressure and photothermal forces[22, 24, 34]. As highlighted in Ref. [34] the photothermal effect is not well described by an energy conserving Hamiltonian formalism owing to its inherently dissipative nature. This is in stark contrast to the well known dispersive optomechanical Hamiltonian, where energy and momentum are conserved by a reversible interaction between optical and mechanical degrees of freedom.

A. General theoretical treatment

Using an approach similar to that taken in Ref. [34] the dispersive optomechanical Hamiltonian is represented in the Heisenberg picture including coupling to a "bath" of resonators that introduces both fluctuations and dissipation into the system. Similarly the photothermal effect is introduced as a fluctuating force with temporal correlations generated by the thermal response to the random absorption of photons. The quantum Langevin equation for the oscillator position $x(t)$ is:

$$m_{\text{eff}}\left[\ddot{x}(t)+\Gamma_m\dot{x}(t)+\omega_m^2 x(t)\right] = F_{RP}+F_{PT}+F_{th} \tag{5}$$

$$= \hbar g\left[a(t)^\dagger a(t)+\frac{\beta A}{\tau_t}\int_{-\infty}^{t}\mathrm{d}u\, e^{-\frac{t-u}{\tau_t}}a(u)^\dagger a(u)\right] + \sqrt{2\Gamma_m m_{\text{eff}} k_b T}\,\xi(t) \tag{6}$$

where A is the absorption coefficient given by the ratio of absorbed to circulating optical power and τ_t is the thermal response time. The dimensionless parameter β quantifies the relative strength of the photothermal process over the radiation pressure such that $F_{PT} = \beta A F_{RP}$. As will be discussed later the absolute value and even the sign of β is strongly dependent on the spatial overlap of the optical and mechanical mode. The intracavity field is dispersively coupled to the mechanical motion so the quantum Langevin equation for the annihilation operator $a(t)$ is :

$$\dot{a}(t) = -\left[\kappa - i\left(\Delta^0 + g x(t)\right)\right]a(t)+\sqrt{2\kappa_{in}}a_{in}(t) \tag{7}$$

where the optomechanical coupling is g, Δ^0 is the optical detuning, and the cavity decay is $\kappa = \kappa_{in}+\kappa_0$. It is useful to note that photothermal backaction is enabled by the temporal delay of the thermal response τ_t in (6), and not the cavity induced delay as in standard dispersive optomechanics. As such, for photothermal cooling the condition of being "resolved" considers

DOI: 10.1038/NPHYS3714

only the thermal response time, hence relaxing the stringent requirements on minimizing the optical decay rate.

To expand the equations of motion into linear and nonlinear components the position and intracavity field annihilation operator are expressed as a coherent amplitude with quantum fluctuations i.e. $x = \bar{x}+\delta x(t)$, $a(t) = \alpha+\delta a(t)$ and $a_{in}(t) = \alpha_{in}+\delta a_{in}(t)$. Here we will only consider a linear photothermal and radiation pressure interaction so the nonlinear terms in (6) and (7) become:

$$iga(t)x(t) = ig\left(\alpha\bar{x} + \delta x(t)\alpha + \delta a(t)\bar{x}\right) \tag{8}$$

$$\hbar g a^{\dagger}(t)a(t) = \hbar g\left(|\alpha|^2 + 2\alpha\delta X^{+}(t)\right) \tag{9}$$

where $\delta X^{+}(t) = \frac{1}{2}\left(\delta a^{\dagger}(t) + \delta a(t)\right)$ are amplitude fluctuations of the intracavity field. For simplicity we have chosen the phase of the intracavity field such that $\alpha = \alpha^{*}$. The steady state equation for the optical field is then:

$$\alpha = \frac{\sqrt{2\kappa_{in}}\alpha_{in}}{\kappa - i\Delta} \tag{10}$$

where the cavity detuning is also modified by the static displacement, $\Delta = \Delta^{0}+g\bar{x}$. The linearised equations of motion for the fluctuations are then:

$$\begin{aligned} m_{\text{eff}}\left[\delta\ddot{x}(t) + \Gamma_m\delta\dot{x}(t) + \omega_m^2\delta x(t)\right] &= 2\hbar g\alpha\left[\delta X^{+}(t) + \frac{\beta A}{\tau_t}\left(H(t)e^{-\frac{t}{\tau_t}}\right) * \delta X^{+}(t)\right] \\ &\quad + \sqrt{2\Gamma_m m_{\text{eff}} k_b T}\,\xi(t) \end{aligned} \tag{11}$$

$$\delta\dot{a}(t) = -\left(\kappa - i\Delta\right)\delta a(t) + ig\alpha\delta x(t) + \sqrt{2\kappa_{in}}\delta a_{in}(t) \tag{12}$$

The photothermal integral in (6) has been replaced by a convolution with a Heaviside function $H(t)$ to preserve causality. Transformation into the Fourier domain (i.e. $\mathcal{F}\{\delta x(t)\} = \delta x$) yields:

$$\delta x = 2\chi(\omega)\hbar g\alpha\delta X^{+}\left[1 + \frac{\beta A}{1 + i\omega\tau_t}\right] \tag{13}$$

$$\delta a = \frac{ig\alpha\delta x + \sqrt{2\kappa_i}\delta\alpha_i}{D(\omega)} \tag{14}$$

which uses the Fourier identity $\mathcal{F}\{H(t)e^{t/\tau_t}\} = \frac{\tau_t}{1+i\tau_t\omega}$, reducing the functional form of the photothermal force to a low pass filter with a corner frequency defined by the characteristic thermalization time. For brevity the mechanical and optical transfer functions have been introduced, $\chi(\omega)^{-1} = m_{\text{eff}}\left(\omega_m^2 - \omega^2 + i\omega\Gamma_m\right)$ and $D(\omega) = \kappa + i(\omega - \Delta)$ respectively. From (13) it is clear

both optomechanical effects arise from intracavity amplitude fluctuations δX^+ which can be expressed as:

$$\delta X^+ = \frac{1}{2}\left(\delta a^\dagger(-\omega) + \delta a(\omega)\right) \tag{15}$$

$$= \frac{\alpha \delta x}{x_{\text{ZPF}} D(\omega) D^*(-\omega)}\left[- \Delta g_0 + \mathcal{O}\{\delta a_{in}\}\right] \tag{16}$$

where the optomechanical coupling rate has been normalized by the oscillators' zero point motion (x_{ZPF}), that is $g_0 = g x_{\text{ZPF}}$, and the fluctuations of the injected optical field have been grouped into a single term $\mathcal{O}\{\delta a_{in}\}$. In the case of a coherent optical drive this term quantifies the additional thermomechanical noise generated by optical vacuum fluctuations, commonly known as quantum backaction. Here, we discard the term $\mathcal{O}\{\delta a_{in}\}$ since dynamical instabilities and thermal noise greatly exceed quantum backaction. Substituting the resulting intracavity amplitude fluctuations into (13) gives:

$$\delta x = \chi(\omega)\left\{ \frac{-4 g_0^2 |\alpha|^2 \omega_m \delta x m_{\text{eff}} \Delta}{D(\omega) D^*(-\omega)}\left[1 + \frac{\beta A}{1 + i\omega\tau_t}\right] + \sqrt{2\Gamma_m m_{\text{eff}} k_b T}\right\} \tag{17}$$

$$= \chi'(\omega)\sqrt{2\Gamma_m m_{\text{eff}} k_b T} \tag{18}$$

where we have made the substitutions $x_{\text{ZPF}}^2 = \hbar / 2 m_{\text{eff}} \omega_m$. The modified mechanical susceptibility $\chi'(\omega)$ includes the radiation pressure and photothermal optomechanical coupling and can be written in the form $\chi'(\omega)^{-1} = m_{\text{eff}}(\omega_m^2 + 2\omega\delta\omega_m - \omega^2 + i\omega[\Gamma_m + \delta\Gamma_m])$. Isolating real and imaginary terms gives the modification to the mechanical resonance frequency $\delta\omega_m$ and decay rate $\delta\Gamma_m$ as:

$$\delta\omega_m = \frac{A(\omega)}{2\omega_m}\left\{\left[(\kappa^2 + \Delta^2 - \omega^2)\left(1 + \frac{\beta A}{1 + \omega^2\tau_t^2}\right) - \frac{2\kappa\omega^2\tau_t \beta A}{1 + \omega^2\tau_t^2}\right]\right\} \tag{19}$$

$$\delta\Gamma_m = -A(\omega)\left\{\left[(\kappa^2 + \Delta^2 - \omega^2)\frac{\tau_t \beta A}{1 + \omega^2\tau_t^2} + 2\kappa\left(1 + \frac{\beta A}{1 + \omega^2\tau_t^2}\right)\right]\right\} \tag{20}$$

where $A(\omega) = \frac{4 g_0^2 |\alpha|^2 \omega_m \Delta}{|D(\omega) D^*(-\omega)|^2}$ is proportional to the magnitude of the cavity response.

Despite extensive experimental work on linear dispersive optomechanics over the last decade the photothermal effect has not received the same level of interest, potentially due to the perceived

DOI: 10.1038/NPHYS3714

limitations of its inherently dissipative origin. To illustrate the nature of photothermal coupling we take the limit where it dominates over radiation pressure, namely $\beta A \gg 1$. In this situation two distinct regimes can be realised depending on the thermalization rate τ_t. As previously mentioned the thermal response can be represented by a low pass filter with corner frequency $1/\tau_t$. If the corner frequency is larger than ω_m then the dominant effect is a shift in the mechanical resonance frequency. Conversely if the corner frequency is less than ω_m then the resulting delay in the photothermal force leads primarily to a modified mechanical decay rate. These two scenarios are analogous to the picture of "unresolved" and "resolved" dynamics in dispersive optomechanics respectively.

B. Proposed mechanism for photothermal actuation

In the superfluid optomechanical system described in this work the photothermal coupling originates from the superfluid fountain effect where superfluid is known to flow towards a localized heat source [35]. In Ref. [36] it has been shown that optical heating around the perimeter of a microtoroidal cavity generates a superfluid thin-film flow up the toroid pedestal and radially outwards towards the toroid perimeter, with the mass-flow balanced by an equivalent level of helium evaporation. It was further shown that intensity modulation of the optical field at the resonance frequency of an intrinsic microtoroid mechanical mode (a mode of the silica structure rather than the superfluid modes studied herein) allowed the microtoroid mode to be coherently driven via a form of photoconvective actuation, where momentum is transferred by recoil of evaporating atoms to the motion of the microtoroid. While as yet we do not have a complete picture of the actuation mechanism that allows both the coherent actuation of superfluid third sound modes and dynamical heating and cooling observed here, we expect that the mechanism is similar to that in Ref. [36].

In general, a third sound wave can be actuated by creating a flow of superfluid with flow field that overlaps the flow field of the third sound wave. This can achieved, for instance, by applying localised heating with a distribution that matches the shape of the third sound wave. In this case, the actuation can be understood through reference to the theoretical description of third sound by Atkins[3]. In thin superfluid films, the normal fluid component of the film is viscously clamped to the surface while the superfluid component can flow. If a third sound wave is excited to some amplitude, much like gravity on a shallow wave wave, van der Waals forces will work to restore the film to a steady-state with uniform height and therefore minimum potential energy. Without

dissipation, the kinetic energy of the flow will, as usual for an oscillator, cause an overshoot from this minimum energy state, and a consequential third sound oscillation. As a result, the superfluid component of the film flows backwards and forwards predominantly in the horizontal direction at the frequency of the third sound wave. If heat is applied to the film in some distribution, the response of the superfluid is to flow towards hotter regions. A heat distribution that is spatially periodic with the wavelength of the third sound wave and oscillates at its resonant frequency will cause a superfluid flow field with spatial structure that overlaps the flow field of the third sound wave. It will therefore create a self-reinforcing oscillation where the superfluid flow generated in each period of third sound oscillation constructively interferes with the flow field of the third sound wave generated previously, and thereby drive the third sound wave.

While the above actuation mechanism is perhaps the most obvious actuation mechanism for third sound waves, we believe it is likely not to be the mechanism at play in our experiments. The splitting of third sound waves we measure indicates that the third sound modes driven in our experiments are not cylindrically symmetric. Specifically, we expect that as a result of the breaking of cylindrical symmetry due to the observed defect on the top surface of the toroid, each third sound mode contains at least one node in the radial direction, and therefore that the direction of circumferential fluid flow alternates around the rim of the toroid[45]. This is supported by the observation in the main text (Fig. 4) that near-degenerate modes are driven very differently by photoconvective forces which, one would expect, would not be the case if the modes were indeed cylindrically symmetric. For the above mechanism to drive such a mode, the optical absorption around the circumference of the toroid would necessarily be non-uniform – perhaps being periodic with wavelength approximately matching the third sound wavelength, or a sub-harmonic of it, or with localised heating at a single defect. There is no reason to think that the optical heating would be periodic. A localised defect is, however, a realistic scenario, for instance if a dust particle was present within the optical mode. Such a defect could, most certainly, allow driving of superfluid modes. However, to explain the large difference between the magnitude of driving of near-degenerate modes, the azimuthal position of the defect would need to closely match the position of the observed defect (main text Fig. 1b (inset)) which breaks the degeneracy of the third sound modes (but does not lie within the optical field and therefore would not, itself, cause optical heating). While we cannot rule this out it would seem somewhat unlikely.

An alternative explanation for photoconvective driving of the superfluid motion takes the realistic assumption that the optical heating is uniform around the circumference of the microtoroid,

DOI: 10.1038/NPHYS3714

but generates a flow field that is non-uniform and overlaps differently with near-degenerate modes. The observed defect that breaks the cylindrical symmetry of the third sound modes to create pairs of symmetric and anti-symmetric modes, will also break the cylindrical symmetry of the superfluid flow. From the optical microscope image of Fig. 1b(inset) of the main text, the diameter of the defect can be seen to be in the range of 2 μm, sufficiently large to have a considerable influence on the flow field of a superfluid film of sub 10 nm thickness, and within a factor of three of the minor diameter of the toroid. Including the presence of the defect and assuming the optical heating is uniform around the toroid circumference, the superfluid flow field will have reflection symmetry about a plane enclosing the defect and the axis of the toroid. One of each pair of near-degenerate third sound modes will match this symmetry and therefore have non-zero overlap with the flow field, while the other – being anti-symmetric – will in principle have zero overlap. We see, therefore, that even with uniform heating around the perimeter of the toroid it is possible, due to breaking of symmetry by the defect, to actuate third sound waves and to postulate an explanation for the very considerable difference in the effectiveness of the actuation on near-degenerate third sound modes. We would emphasis, however, that to reach a concrete conclusion regarding the exact mechanism of photoconvective driving will require further experimentation with different resonator geometries for which the superfluid flow field and third sound modes can be modelled precisely, work that is beyond the scope of the present paper.

VII. REAL-TIME POSITION MEASUREMENT OF AN OSCILLATOR

Here we consider an oscillator under continuous measurement. We re-derive well-known results from the quantum and classical control communities (for example, see [37–41]) for the conditional evolution of the oscillator, given knowledge obtained from the measurement. This will allow the rate at which the measurement reduces the variance of the oscillator to be determined. This rate identifies a natural timescale associated with the measurement, and is conventionally termed the *measurement rate*, and allows physically different measurement regimes to be identified[42, 43]. In general, those regimes include a *weak measurement regime*, where the measurement is insufficient to resolve even the thermal motion of the oscillator – this is the regime in which all previous superfluid measurements have resided, a *real-time measurement regime*, where the measurement is sufficient to resolve, track, and control the thermal motion of the oscillator but does not introduce significant quantum back-action noise – this is the regime of the experiments performed in this

paper, and a *quantum measurement regime*, where quantum back-action noise dominates. Here, we follow the derivation of Refs. [42, 43]. The results that follow are summarised illustratively in the Fig. 10 below.

The measurement rate, once determined, will be linked to the signal-to-noise ratio of spectral analysis via a quantum Langevin model.

While we use an open quantum systems approach to model this system, we note that in the classical regime in which our experiments operate, a classical stochastic model would work equally well.

A. Conditional variance of an oscillator under continuous measurement

The unitary dynamics of a harmonic oscillator are, of course, described by the Hamiltonian

$$\hat{H} = \frac{k\hat{x}^2}{2} + \frac{\hat{p}^2}{2m_{\text{eff}}} = \hbar\omega_m b^\dagger b, \tag{21}$$

where $\hat{x}$ and $\hat{p}$ are, respectively, the oscillators position and momentum operators, m_{eff} is its effective mass, ω_m its resonance frequency, $k = m_{\text{eff}}\omega_m^2$ its spring constant, and b and $b^\dagger$, respectively its annihilation and creation operators which obey the commutation relation $[b, b^\dagger] = 1$.

We wish to consider the specific case of a high quality oscillator, by which we mean that the frequency of the oscillator ω_m is much greater than its damping rate Γ_m, and is also much greater than the measurement rate to be determined later. This is the usual regime for cavity optomechanics experiments, and is the regime in which the experiments reported here operate. In this regime it is natural to move into a frame rotating at the mechanical resonance frequency. In the rotating frame (or equivalently, in the interaction picture) the Hamiltonian is rather uninteresting:

$$\hat{H}_I = 0. \tag{22}$$

That is to say, in this frame, the unitary dynamics of the oscillator are frozen, though of course it still interacts with its environment via both thermal driving and damping. It is, further, natural to define the quadrature operators:

$$\hat{X}(t) \equiv \frac{1}{\sqrt{2}}\left(b^\dagger e^{i\omega_m t} + b e^{-i\omega_m t}\right) \tag{23a}$$

$$\hat{Y}(t) \equiv \frac{i}{\sqrt{2}}\left(b^\dagger e^{i\omega_m t} - b e^{-i\omega_m t}\right). \tag{23b}$$

DOI: 10.1038/NPHYS3714

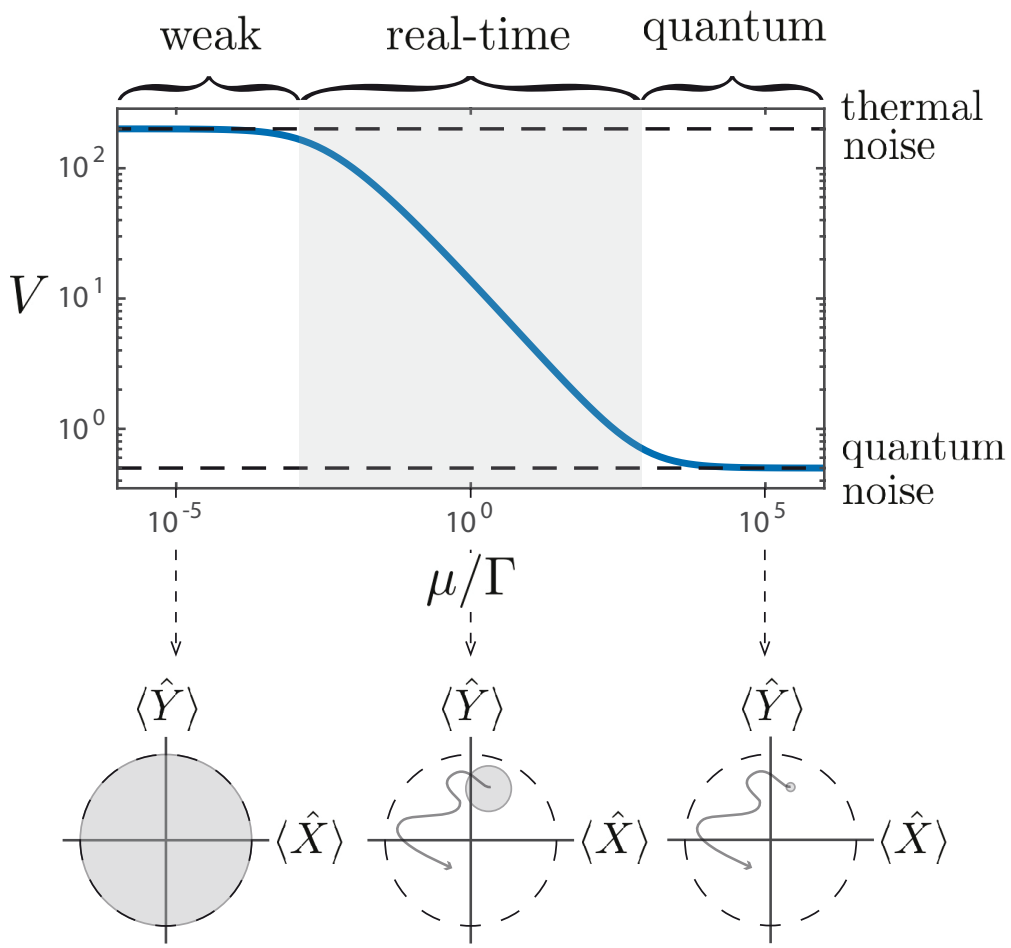

FIG. 10: **Mechanical oscillator measurement regimes.** Conditional variance V of the quadratures of a mechanical oscillator under continuous measurement as a function of measurement rate μ, showing the weak, real-time, and quantum measurement regimes of operation. Here, Γ_m is the decay rate of the oscillator. Parameters: $\eta = 1$, $\bar{n} = 200$. The phasor diagrams beneath the main figure show the knowledge gained from the measurement about the position of the oscillator in phase space. The dashed circles represent the thermal noise variance of the oscillator, while the grey circles represent the standard deviation of the quadrature estimates. The left plot is will inside the weak measurement regime, with $\mu/\Gamma_m = 10^{-5}$ and shows that the measurement provides no information about the dynamics of the oscillator. The centre plot is in the real-time measurement regime, with $\mu/\Gamma_m = 1$, showing that the measurement is able to localise the oscillator in phase space, and therefore track its real-time dynamics. The right trace is in the quantum measurement regime, with $\mu/\Gamma_m = 10^5$, with the uncertainty in the localisation of the oscillator limited by quantum back-action noise. The curved arrows schematically illustrate a trajectory on which the thermal (and back-action) may drive the oscillator.

The essential idea here, is that $\hat{X}(t)$ follows the original position of the oscillator (at time $t = 0$) as it rotates into momentum, while $\hat{Y}(t)$ similarly follows the oscillators original momentum. For a high quality oscillator (as defined above) a measurement of the position $\hat{x}$ of the oscillator can accurately be treated as two independent measurements of of $\hat{X}$ and $\hat{Y}$ (see, for example, Ref. [42]). We envisage a continuous measurement of the position of the oscillator, which results in quadrature photocurrents:

$$i_X(t)dt = \frac{\mu^{1/2}}{2}\langle\hat{X}\rangle dt + dW_X(t) \tag{24a}$$

$$i_Y(t)dt = \frac{\mu^{1/2}}{2}\langle\hat{Y}\rangle dt + dW_Y(t) \tag{24b}$$

where here μ is normalised appropriately – as we will see later – so as to equal the measurement rate, and $dW_X(t)$ and $dW_Y(t)$ are, respectively, the usual infinitesimal Wiener increments for the X- and Y-quadratures, which should be understood to be uncorrelated unit Gaussian white noise processes which quantify the precision of the measurement and, among other properties, satisfies $dW_X^2(t) = dW_Y^2(t) = dt$. This *Itō rule* is a key property of Itō stochastic calculus. It may seem strange, since the Wiener increments are white noise and dt is deterministic. However, it is valid due to the fact that Wiener increments are ultimately always evaluated within integrals[39]. In usual calculus, one keeps only terms that are constant or linear in the increment (e.g., dt^2 would be neglected). In Itō calculus, the second order terms must also be kept, since they are first order in dt. We refer the reader to Ref. [39] for more discussion of Itō calculus.

Note that the equations above are not written as the usual derivatives (i.e. $\frac{di}{dt}$) since, formally, the derivatives of Wiener increments are not well defined. The complete evolution of of the conditional density matrix[46] ρ is then determined by the stochastic master equation

$$\begin{aligned} d\rho &= \Gamma_m(\bar{n}+1)\mathcal{D}[\hat{b}]\rho\,dt + \Gamma_m\bar{n}\mathcal{D}[\hat{b}^\dagger]\rho\,dt \\ &+\frac{\mu^{1/2}}{2}\left[\eta^{-1/2}\mathcal{D}[\hat{X}]\rho\,dt + \eta^{-1/2}\mathcal{D}[\hat{Y}]\rho\,dt + \mathcal{H}[\hat{X}]\rho\,dW_X + \mathcal{H}[\hat{Y}]\rho\,dW_Y\right], \end{aligned} \tag{25}$$

where $\bar{n} \approx k_B T/\hbar\omega_m$ is the thermal occupancy of the bath coupled to the mechanical oscillator at rate Γ_m, $\hat{b}$ and $\hat{b}^\dagger$ are the annihilation and creation operators for the mechanical oscillator in the rotating frame, η is the measurement efficiencies including losses and also optical and technical noise that increases the measurement noise floor above the quantum noise limit, and $\mathcal{D}$ and $\mathcal{H}$ are

DOI: 10.1038/NPHYS3714

the Lindblad and measurement superoperators defined by

$$\mathcal{D}[\hat{\mathcal{O}}]\rho \equiv \hat{\mathcal{O}}\rho\hat{\mathcal{O}}^\dagger - \frac{1}{2}\left(\hat{\mathcal{O}}^\dagger\hat{\mathcal{O}}\rho + \rho\hat{\mathcal{O}}^\dagger\hat{\mathcal{O}}\right) \tag{26a}$$

$$\mathcal{H}[\hat{\mathcal{O}}]\rho \equiv \hat{\mathcal{O}}\rho + \rho\hat{\mathcal{O}}^\dagger - \left\langle \hat{\mathcal{O}} + \hat{\mathcal{O}}^\dagger \right\rangle \rho, \tag{26b}$$

with $\hat{\mathcal{O}}$ being an arbitrary operator. The "$\mathcal{D}$" terms in Eq. (25) represent the heating due to the thermal environment of the mechanical oscillator and the quantum back-action from the measurement. While the experiments reported in the main text do not exhibit observable quantum back-action, the terms are important here to establish the measurement rate. As can be seen, as the efficiency of the measurement diminishes the back-action heating increases for a fixed measurement rate μ. The "$\mathcal{H}$" terms account for the oscillator localisation due to knowledge gained through the measurement.

Using Eq. (25) the evolution of the expectation values and variance of the X- and Y-quadratures of the oscillator may be determined, as usual, via

$$d\langle\hat{\mathcal{O}}\rangle = \mathrm{Tr}\left[\hat{\mathcal{O}}\, d\rho\right], \tag{27}$$

where $\mathrm{Tr}[\hat{\mathcal{O}}\, d\rho]$ is the trace and $\hat{\mathcal{O}}$ is some arbitrary operator.

Following Ref. [42] and using the definitions of the Wiener increments in terms of photocurrents in Eqs. (24), we find:

$$\frac{d\langle\hat{X}\rangle}{dt} = -\frac{1}{2}\left(\Gamma_m + \mu V\right)\langle\hat{X}\rangle - \frac{\mu}{2}C_{XY}\langle\hat{Y}\rangle + \mu^{1/2}V\, i_X + \mu^{1/2}C_{XY}\, i_Y \tag{28a}$$

$$\frac{d\langle\hat{Y}\rangle}{dt} = -\frac{1}{2}\left(\Gamma_m + \mu V\right)\langle\hat{Y}\rangle - \frac{\mu}{2}C_{XY}\langle\hat{X}\rangle + \mu^{1/2}V\, i_Y + \mu^{1/2}C_{XY}\, i_X, \tag{28b}$$

where, $V \equiv \langle\hat{X}^2\rangle - \langle\hat{X}\rangle^2 = \langle\hat{Y}^2\rangle - \langle\hat{Y}\rangle^2$ is the conditional variance of both the X- and the Y-quadrature, which – since the measurement is continuous and unbiased – turn out to be equal, and $C_{XY} \equiv \langle\hat{X}\hat{Y} + \hat{Y}\hat{X}\rangle/2 - \langle\hat{X}\rangle\langle\hat{Y}\rangle$ is their covariance. We see here that, as must be the case, when there is no measurement, the expectation values of the quadratures decay at a rate dictated by Γ_m. The introduction of quadrature measurements *increases* the (conditional) decay rates of both quadratures by the product of the variance and the measurement rate μ, as the expectation values become better determined. However, as can be seen, they also introduce diffusion (the terms proportional to i_X and i_Y). This diffusion arises because, if a measurement at time t indicates that the oscillator is localised at a different place in phase space than the prior measurements, the expectation value of the quadratures must be corrected.

Equations (28) are easily solved in the frequency domain in the usual long-time limit where the quadrature conditional variances have reached steady-state. In this limit $C_{XY} = 0$, as might be expected[42]. Taking the Fourier transforms of Eqs. (28) one then finds straightforwardly that the optimal estimate of $\langle\hat{X}\rangle$ and $\langle\hat{Y}\rangle$ are

$$\langle\hat{X}\rangle(\omega) = h(\omega)i_X(\omega) \tag{29a}$$

$$\langle\hat{Y}\rangle(\omega) = h(\omega)i_Y(\omega), \tag{29b}$$

where the filter function $h(\omega)$ is defined as

$$h(\omega) \equiv \frac{\sqrt{\mu}}{(\Gamma_m + \mu V)/2 - i\omega} \tag{30}$$

Using Eqs. (25) and (27), we can find equations of motion for the quadrature conditional variances and covariance in a similar manner to the quadrature expectations values, above. The conditional variance is a particularly experimentally relevant parameter – it quantifies the uncertainty in the estimate of the quadratures in Eqs. (29). Without any measurement, the conditional variance equals the thermal variance $\bar{n} + 1/2$. As the measurement strength increases, one expects the conditional variance to reduce, allowing the oscillator to be tracked in phase space. Assuming Gaussian statistics, as is appropriate for an oscillator driven by thermal noise, the result[42] is that, in the long-time limit the covariance $C_{XY} = 0$, as might be expected; while the quadrature variances evolve independently according to the equation of motion

$$\dot{V} = -\Gamma_m V - \mu V^2 + \Gamma_m \left(\bar{n} + \frac{\mu}{4\eta\Gamma_m} + \frac{1}{2}\right) \tag{31}$$

We see that, of course, the variances decay into the bath with a rate Γ_m – this is just the energy decay of the oscillator – and are also driven by the bath fluctuations, as expected from the fluctuation-dissipation theorem. More interesting, is the effect of the measurement. As can be seen, the measurement introduces additional nonlinear damping of each quadrature variance, equal to the variance squared scaled by the measurement rate μ. It, further, introduces back-action heating proportional to μ and inversely proportional to the detection efficiency η. Solving this equation in the steady-state ($\dot{V} = 0$), we find

$$V = \sqrt{\left(\frac{\Gamma_m}{2\mu}\right)^2 + \frac{\Gamma_m}{\mu}\left(\bar{n} + \frac{1}{2}\right) + \frac{1}{4\eta}} - \frac{\Gamma_m}{2\mu}. \tag{32}$$

DOI: 10.1038/NPHYS3714

As discussed above, this equation has three distinct parameter regimes. In the quantum measurement regime defined by $\mu > \{\Gamma_m/\eta, 4\eta\Gamma_m(\bar{n}+1/2)\}$, the quadratures of the oscillator are determined by the measurement at a rate much faster than the thermal decoherence rate. Here, the mechanical dynamics are quantum back-action dominated with the final conditional variance independent of the bath occupancy and equal to $V \sim 1/2\eta^{1/2}$. In the real-time measurement regime, $\Gamma_m/[4(\bar{n}+1/2)] < \mu < 4\eta\Gamma_m(\bar{n}+1/2)$. Here the measurement rate remains faster than the thermal decoherence rate, but not sufficiently fast that the thermal driving is entirely frozen out. The conditional variances are then[47]

$$V \sim \sqrt{\frac{\Gamma_m}{\mu}\left(\bar{n}+\frac{1}{2}\right)} < \bar{n}+\bar{n}_{ba}+\frac{1}{2}, \tag{33}$$

where $\bar{n}_{ba} = \mu/4\eta\Gamma_m$ is the back-action heating of the mechanical oscillator due to the measurement. In most situations, and certainly for the measurements reported in this paper, this back-action heating term is negligible. We see from Eq. (33) that in the real-time measurement regime, and neglecting back-action heating, the measurement localises the quadrature variances of the oscillator to beneath the thermal variance. Finally, in the weak measurement regime, defined by $\mu < \Gamma_m/[4(\bar{n}+1/2)]$ in the usual situation where the efficiency $\eta \gg (2\bar{n}+1)^{-2}/4$, the thermal decoherence rate dominates with $V \sim \bar{n}+1/2$. The conditional variance V is plotted as a function of measurement rate μ in Fig 10, showing the distinct transition between the three measurement regimes.

As we have seen in the above argument, the measurement rate

$$\mu_{\text{threshold}} = \frac{\Gamma_m}{4(\bar{n}+1/2)} \tag{34}$$

defines a threshold, below which the conditional variances of the mechanical oscillator are constrained to approximately the thermal variance, and above which, the measurement becomes sufficiently strong as to overcome the thermal heating and localise the oscillator to beneath the thermal variance. Such capabilities are crucial, not only to be able to control the motion of the oscillator – for instance to cool it – but also to simply track its motion in real-time. Representing the oscillator, as usual, as a phasor in X-Y space, it is clear that, to determine the length and orientation of the vector, one must be able to resolve its location to better than the mechanical thermal variance. Hence, the criterion in Eq. (34) defines the transition between a measurement that is capable of real-time tracking of the oscillator dynamics and one that is not. All previous measurements of sound waves in superfluid have been constrained to the weak measurement regime.

B. Mechanical power spectral density

The measurement rate in Eq. (34) can be related to the signal-to-noise ratio of the peak of the mechanical power spectrum to the noise floor of the power spectral density. Here, we establish that link using a quantum Langevin approach. We wish to consider a system consisting of an optical cavity dispersively coupled to the position of a mechanical oscillator. In a linearised picture where the optical drive field is bright and the optomechanical coupling not strong enough that a single photon substantially alters the dynamics of the mechanical oscillator, such a system is well described by the standard Hamiltonian

$$\hat{H} = \hbar\omega_m b^\dagger b + 2\hbar g \hat{X}_L \hat{Q} \tag{35}$$

where we have moved into a frame for the optical field rotating at the optical cavity resonance frequency such that no bare cavity Hamiltonian is present here, g is the usual coherent amplitude boosted optomechanical coupling rate, $\hat{Q} = (b^\dagger + b)/\sqrt{2}$ is the dimensionless mechanical position operator, and $\hat{X}_L$ is the amplitude quadrature of the optical field, with the optical amplitude and phase ($\hat{Y}_L$) quadratures satisfying the commutation relations $[\hat{X}_L, \hat{Y}_L] = i$.

Using the standard quantum Langevin approach (see e.g. [44] we arrive at the equations of motion

$$\dot{\hat{X}}_L = -\frac{\kappa}{2}\hat{X}_L + \sqrt{\kappa}\hat{X}_{L,\mathrm{in}} \tag{36a}$$

$$\dot{\hat{Y}}_L = -\frac{\kappa}{2}\hat{Y}_L + \sqrt{\kappa}\hat{Y}_{L,\mathrm{in}} - 2g\hat{Q} \tag{36b}$$

$$\ddot{\hat{Q}} + \Gamma_m\dot{\hat{Q}} + \omega_m^2\hat{Q} = \sqrt{2\Gamma_m}\omega_m\hat{P}_{\mathrm{in}} - 2g\omega_m\hat{X}. \tag{36c}$$

where κ is the optical decay rate, $\hat{X}_{L,\mathrm{in}}$ and $\hat{Y}_{L,\mathrm{in}}$ are input noise operators for the optical phase and amplitude quadratures, which we take without loss of generality to be shot noise limited so that their symmetrised power spectral densities $\bar{S}_{X_{L,\mathrm{in}}X_{L,\mathrm{in}}}(\omega) \equiv (S_{X_{L,\mathrm{in}}X_{L,\mathrm{in}}}(\omega) + S_{X_{L,\mathrm{in}}X_{L,\mathrm{in}}}(-\omega))/2 = 1/2$ and $\bar{S}_{Y_{L,\mathrm{in}}Y_{L,\mathrm{in}}}(\omega) = 1/2$, and $\hat{P}_{\mathrm{in}}$ is the input noise operator describing the force applied to the mechanical momentum quadrature, which has a symmetrised power spectral density $\bar{S}_{P_{\mathrm{in}}P_{\mathrm{in}}}(\omega) = \bar{n} + 1/2$.

Taking the Fourier transform of Eq. (36c) and calculating the power spectral density of the resulting frequency domain solution for $\hat{Q}$ yields the symmetrised power spectral density

$$\bar{S}_{QQ}(\omega) = 2\Gamma_m|\chi(\omega)|^2\left(\bar{n} + \bar{n}_{ba} + 1/2\right), \tag{37}$$

DOI: 10.1038/NPHYS3714

where $\chi(\omega) \equiv \omega_m/(\omega_m^2 - \omega^2 - i\omega\Gamma_m)$ is the mechanical susceptibility, which quantifies the frequency response of the mechanical resonator to external forces, and

$$\bar{n}_{\rm ba} = \frac{4g^2}{\kappa\Gamma_m} \times \frac{1}{1+4(\omega_m/\kappa)^2} \tag{38}$$

is the (unavoidable in a continuous measurement) quantum back-action heating introduced to the mechanical oscillator from the measurement, where the first term is the usual cooperativity, and the second term quantifies the reduction in radiation pressure driving due to the sidebands being partially off-resonance with the cavity. In obtaining this result, we have also assumed that the factor $f(\omega) = 1+4(\omega/\kappa)$ is well approximated as constant over the frequency range that contains appreciable mechanical power. This is a reasonable assumption for a high quality mechanical oscillator.

It is now possible to relate the measurement rate μ to the back-action heating rate $\bar{n}_{ba}$, and therefore the usual optomechanical parameters, through comparison of Eqs. (31) and (37). Specifically, we find

$$\mu = 4\eta\Gamma_m\bar{n}_{ba} = \frac{16\eta g^2}{\kappa} \times \frac{1}{1+4(\omega_m/\kappa)^2}. \tag{39}$$

To determine the signal-to-noise ratio (SNR) of a measurement of the output field of the cavity, we solve Eq. (36b) for the phase quadrature of the intracavity field, again by taking a Fourier transform, and use the input-output relations[44] to find the phase quadrature of the output field[48]:

$$\hat{Y}_{L,\rm out}(\omega) = -\left(\frac{\kappa/2+i\omega}{\kappa/2-i\omega}\right)\hat{Y}_{L,\rm in}(\omega) + 2\sqrt{\Gamma_m\bar{n}_{\rm ba}}\hat{Q}(\omega). \tag{40}$$

Including detection inefficiency η, $\hat{Y}_{L,\rm out} \to \sqrt{\eta}\hat{Y}_{L,\rm out} + \sqrt{1-\eta}\hat{Y}_{L,\rm vac}$, where $\hat{Y}_{L,\rm vac}$ is the phase quadrature of vacuum noise entering through the loss port, with $\bar{S}_{Y_{L,\rm vac}Y_{L,\rm vac}}(\omega) = 0$. Note that this inefficiency has the role, only, of decreasing the signal-to-noise of the measurement, and can therefore be equally well used to model effects such as detector dark noise. The symmetrised power spectral density of the phase quadrature is then

$$\bar{S}_{Y_{L,\rm out}Y_{L,\rm out}}(\omega) = \frac{1}{2} + 4\eta\Gamma_m\bar{n}_{\rm ba}\bar{S}_{QQ}(\omega). \tag{41}$$

The signal-to-noise ratio, defined as the ratio of the power spectral density at the peak of the mechanical mode ($\omega = \omega_m$) to the optical noise floor of the measurement, is therefore

$$\begin{aligned} {\rm SNR} &= 8\eta\Gamma_m\bar{n}_{\rm ba}\bar{S}_{QQ}(\omega_m) && (42)\\ &= 4\left(\bar{n}+\bar{n}_{ba}+1/2\right)\frac{\mu}{\Gamma_m}. && (43) \end{aligned}$$

Taking the limit relevant to our experiments, where $\bar{n}_{ba} \ll \bar{n}$, i.e., the back-action noise is insignificant, we have

$$\mathrm{SNR} = \frac{4(\bar{n} + 1/2)}{\Gamma_m}\mu. \tag{44}$$

Substituting the threshold measurement rate from Eq. (34), we can determine the threshold signal-to-noise ratio required to reach the real-time measurement regime:

$$\mathrm{SNR}_{\mathrm{threshold}} = 1. \tag{45}$$

So we discover that the threshold to reach the real-time measurement regime is exactly a signal-to-noise ratio of unity, matching our intuition. Signal-to-noise ratios above this level are required to track the mechanical oscillator dynamics in real-time.

[1] R. J. Donnelly, Physics Today **62**, 34 (2009).

[2] D. Tilley and J. Tilley, *Superfluidity and Superconductivity* (CRC Press, Bristol, 1990).

[3] K. R. Atkins, Physical Review **113**, 962 (1959).

[4] C. W. F. Everitt, K. R. Atkins, and A. Denenste, Physical Review Letters **8**, 161 (1962).

[5] C. W. F. Everitt, Denenste.A, and K. R. Atkins, Physical Review **136**, 1494 (1964).

[6] R. J. Donnelly and C. F. Barenghi, Journal of Physical and Chemical Reference Data **27**, 1217 (1998).

[7] J. H. Scholtz, E. O. McLean, and I. Rudnick, Physical Review Letters **32**, 147 (1974).

[8] S. Wang, K. S. Ketola, P. Lemaire, and R. B. Hallock, Journal of Low Temperature Physics **119**, 645 (2000).

[9] M. P. Lilly, F. Portier, and R. B. Hallock, Physical Review B **63** (2001).

[10] T. McMillan, J. E. Rutledge, and P. Taborek, Journal of Low Temperature Physics **138**, 995 (2005).

[11] A. M. R. Schechter, R. W. Simmonds, R. E. Packard, and J. C. Davis, Nature **396**, 554 (1998).

[12] J. A. Hoffmann, K. Penanen, J. C. Davis, and R. E. Packard, Journal of Low Temperature Physics **135**, 177 (2004).

[13] F. M. Ellis and H. Luo, Physical Review B **39**, 2703 (1989).

[14] A. M. R. Schechter, R. W. Simmonds, and J. C. Davis, Journal of Low Temperature Physics **110**, 603 (1998).

[15] I. White, Thesis (2006).

[16] F. M. Ellis and L. Li, Physical Review Letters **71**, 1577 (1993).

DOI: 10.1038/NPHYS3714

[17] A. Vorontsov and J. A. Sauls, Journal of Low Temperature Physics **134**, 1001 (2004).

[18] L. Ding, C. Baker, P. Senellart, A. Lemaitre, S. Ducci, G. Leo, and I. Favero, Applied Physics Letters **98**, 113108 (2011).

[19] G. Anetsberger, E. M. Weig, J. P. Kotthaus, and T. J. Kippenberg, Comptes Rendus Physique **12**, 800 (2011).

[20] M. L. Gorodetksy, A. Schliesser, G. Anetsberger, S. Deleglise, and T. J. Kippenberg, Optics Express **18**, 23236 (2010).

[21] M. Eichenfield, R. Camacho, J. Chan, K. J. Vahala, and O. Painter, Nature **459**, 550 (2009).

[22] C. H. Metzger and K. Karrai, Nature **432**, 1002 (2004).

[23] C. Metzger, I. Favero, A. Ortlieb, and K. Karrai, Physical Review B **78**, 035309 (2008).

[24] K. Usami, A. Naesby, T. Bagci, B. M. Nielsen, J. Liu, S. Stobbe, P. Lodahl, and E. S. Polzik, Nature Physics **8**, 168 (2012).

[25] T. P. Purdy, R. W. Peterson, and C. A. Regal, Science **339**, 801 (2013).

[26] P. E. Barclay, K. Srinivasan, O. Painter, B. Lev, and H. Mabuchi, Applied Physics Letters **89** (2006).

[27] O. Arcizet, R. Rivière, A. Schliesser, G. Anetsberger, and T. J. Kippenberg, Physical Review A **80**, 021803 (2009).

[28] S. Rips, M. Kiffner, I. Wilson-Rae, and M. J. Hartmann, New Journal of Physics **14**, 023042 (2012).

[29] R. Riviere, O. Arcizet, A. Schliesser, and T. J. Kippenberg, Review of Scientific Instruments **84**, 043108 (2013).

[30] Y. Pramudya, Thesis (2012).

[31] A. A. Clerk, M. H. Devoret, S. M. Girvin, F. Marquardt, and R. J. Schoelkopf, Reviews of Modern Physics **82**, 1155 (2010).

[32] S. M. Meenehan, J. D. Cohen, S. Groblacher, J. T. Hill, A. H. Safavi-Naeini, M. Aspelmeyer, and O. Painter, Physical Review A **90** (2014).

[33] J. M. Pirkkalainen, E. Damskägg, M. Brandt, F. Massel, and M. A. Sillanpää, arXiv:1507.04209 (2015).

[34] J. Restrepo, J. Gabelli, C. Ciuti, and I. Favero, Comptes Rendus Physique **12**, 860 (2011).

[35] J. F. Allen and H. Jones, Nature **141**, 243 (1938).

[36] D. L. McAuslan, G. I. Harris, C. Baker, Y. Sachkou, X. He, E. Sheridan, and W. P. Bowen, arXiv preprint arXiv:1512.07704 (2015).

[37] K. Jacobs and D. A. Steck, Contemporary Physics **47**, 279 (2006).

[38] J. Gough, *Optimal Quantum Feedback for Canonical Observables* (World Scientific, 2012), pp. 262–279.

[39] C. Gardiner, *Stochastic Methods: A Handbook for the Natural and Social Sciences* (Springer Berlin Heidelberg, 2009), ISBN 9783540707127.

[40] K. Jacobs and P. L. Knight, Physical Review A **57**, 2301 (1998).

[41] H. Wiseman and G. J. Milburn, *Quantum measurement and control* (Cambridge University Press, 2009).

[42] A. C. Doherty, A. Szorkovszky, G. I. Harris, and W. P. Bowen, Philosophical Transactions of the Royal Society a-Mathematical Physical and Engineering Sciences **370**, 5338 (2012).

[43] W. P. Bowen and G. Milburn, *Quantum Optomechanics* (CRC Press, 2015), ISBN 9781482259155.

[44] C. Gardiner and P. Zoller, *Quantum Noise: A Handbook of Markovian and Non-Markovian Quantum Stochastic Methods with Applications to Quantum Optics* (Springer, 2004), ISBN 9783540223016.

[45] We would note here that due to the density and complexity of the spectrum of superfluid modes in our experiments (see Section II) even without a defect, we are limited here to symmetry arguments, with numerical simulations proving to be intractable.

[46] Here, the conditional density matrix represents the state of the system given the knowledge gained by the experimenter from the measurement.

[47] Note that there is one significant regime where the inequality below is not valid: when the measurement efficiency is very low, but the quantum back-action is non-negligible. In this case, the quantum back-action heats the oscillator, but the measurement precision is insufficient

[48] We choose the phase quadrature since no information about the mechanical oscillator is contained on the amplitude quadrature.